Seeing through turbidity with harmonic holography [Invited]

Ye Pu* and Demetri Psaltis

Laboratory of Optics, School of Engineering, École Polytechnique Fédérale de Lausanne (EPFL), BM 4.107, Station 17, Lausanne 1015, Switzerland

*Corresponding author: ye.pu@epfl.ch

Received 1 October 2012; accepted 1 October 2012;
posted 4 October 2012 (Doc. ID 177146); published 24 January 2013

The ability to see inside the body noninvasively is indispensable in modern biology and medicine. Optical approaches to such abilities are of rapidly growing interest because of their nonionizing nature and low cost. However, the problem of opacity due to the optical turbidity of tissues must be addressed before optical means become practical. Harmonic holography amalgamates the capability of holographic phase conjugation with the contrast-forming mechanism of second-harmonic generation, which provides a unique opportunity for imaging through a turbid medium. In this review we give accounts of the effort of imaging through turbid media using harmonic holographic phase conjugation.

OCIS codes: 070.5040, 090.1995, 180.4315, 290.4210, 160.4236, 030.6140.

1. Introduction

Since Wilhelm Röntgen discovered x rays in 1895, the ability to see inside the body noninvasively has greatly revolutionized clinical diagnostics. Computed tomography, magnetic resonance imaging, and positron emission tomography have been indispensable tools in virtually every modern hospital. Despite their unquestionable merits, there are growing concerns over the dose of the ionizing radiation [1] and the costs of equipment and operation. In contrast, visible and infrared light in the electromagnetic spectrum is generally nonionizing, provides high resolution, and is easy to generate and detect, which attracted increasing interests in tomographic imaging. Indeed, the past decade has witnessed a fast growth in the number of applications using optical tomography [2,3].

In the optical band, however, a grave challenge to tackle in tomography is the opacity of most biological tissues. The opacity is a result of absorption and scattering by objects covering a wide range of sizes. While absorption clearly leads to irreversible loss of energy and hence information, it was shown in early holographic experiments that information is preserved rather than destroyed through scattering. The effect of scattering is a highly complex remapping of the light distribution resulting in scrambled information. Fortunately, there exists a spectral window, mainly located in the red to near-infrared (NIR) region, in most biological tissues where absorption can be neglected and scattering dominates. Such objects are generally called scattering media. They are also known as turbid media in optics or disordered media in condensed matter physics. Understanding and control of light wave propagation in a scattering medium [4] is therefore of major concern in the effort to see through such media.

Digital phase conjugation with harmonic holography (H^2) [5] is among several emerging techniques for imaging through scattering media. It is a nonlinear optical technique that combines the focusing-through-scattering capability of holographic phase conjugation with the contrast forming ability of second-harmonic generation (SHG). Here we review the problem of imaging through turbid media, with the main focus on the technique enabled by H^2 phase conjugation. Section 2 is devoted to light propagation in a turbid medium and the techniques to extract

1559-128X/13/040567-12$15.00/0

image information from it. In Sections 3 and 4 we explain SHG as a contrast forming mechanism and the materials for such purpose. Sections 5 and 6 present H^2 and its applications in imaging through turbid media through digital phase conjugation. This article is not intended to be a comprehensive review on the topic of optical tomography or wave propagation in turbid media. Excellent reviews and reference materials can be found elsewhere [4,6,7]. Throughout this paper, we use the terms scattering medium, disordered medium, and turbid medium interchangeably.

2. Imaging in Turbid Media

The problem of imaging inside or through turbid media is summarized in Fig. 1. The (coherent) light wave from a source S, which is to be imaged by a lens, enters a disordered medium containing randomly dispersed scatterers, where it undergoes multiple scattering events. The light directly emitted from S, often termed the ballistic photons, loses energy to the scattered light and is extinguished exponentially as $I_{\text{bal}}(z) = I_0 \exp(-z/\ell)$ without considering the cosine of the incident angle. This is known as the Beer–Lambert law. Here I_0 and I_{bal} are the intensity of the incident and the ballistic light, respectively, and z is the propagation distance. ℓ is the scattering length, which indicates the average distance for light wave propagation without being appreciably scattered. It is often considered as the average distance for a photon to travel before encountering a scattering event, and hence the name photon mean free path. Here the photon mean free path ℓ is a crucial parameter that governs the behavior of the scattering medium. If $\ell \gg L$, where L is the thickness of the scattering medium, the ballistic photons transmit through the scattering medium without being significantly extinguished, and the images only suffer a reduced contrast similar to what we might see on a foggy day. If $\lambda \ll \ell \ll L$, known as the diffusive or weak localization regime [6], the incident light is scattered multiple times before reaching the emerging face and loses almost all its power to the scattered light. The scattered light intensity follows a diffusion model. If $\ell \ll \lambda$, the incident light stays in a localized state and does not propagate into the medium, which is a phenomenon first predicted by Anderson [8] and is known as Anderson localization or strong localization. In what follows we focus on the regime of weak localization. We further assume that the absorption in the turbid medium is negligible, which is valid in real biological conditions in the red to NIR band [9].

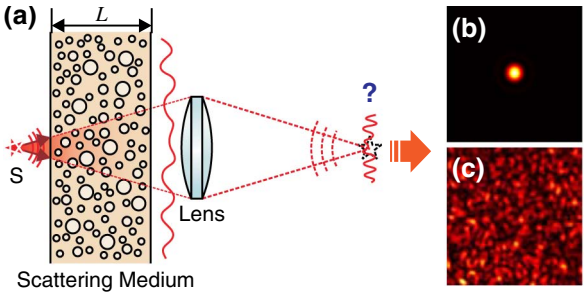

Fig. 1. (Color online) Problem of imaging through turbid media. (a) Light wave from a light source (red star) propagates through a disordered scattering medium of thickness L and undergoes multiple scattering events that destroy its spatial coherence before reaching the imaging lens. (b) In the absence of the scattering medium, the light from the source focuses as a converging spherical wave (dashed arcs), forming an image (black dashed star) as shown. (c) Due to the scattering in the turbid medium, which decimates the direct transmitted wave (the ballistic photons), and the highly distorted wave (red wavy curves) emerging from the turbid medium does not form an image but rather spreads into a speckle field, as shown. At question is how to retrieve an image of the source S from the speckle.

The information on the incident wave is, however, not all forgotten. It has been shown, theoretically [10] and experimentally [11], that some information is remembered (or transmitted) by the emerging wave in spite of the disorder. More specifically, if the incident wave is subject to a linear phase shift that is equivalent to a wavefront rotation of an angle θ around an axis in the transverse plane, there is a nonzero intensity-intensity correlation between the emerging wavefronts before and after the rotation. This correlation, called the "memory effect", is expressed as $C(\theta) = (k\theta L/\sinh k\theta L)^2$, where $k = 2\pi/\lambda$ is the wavenumber. In a Fourier sense, this equation suggests that the angular bandwidth of an image transmitted through the scattering medium is limited by $\theta_{\max} \sim (1/kL)$, which leads to a resolution limit of $\sim L$. Hence, spatial intensity features of the incident wave larger than the thickness of the medium do survive the scattering. This can often be used to directly image through the scattering medium under proper imaging conditions.

In the weak localization (diffusive) regime, the wave emerging from the scattering medium is a random intensity map of large fluctuations, which is well known as speckle in optics. The speckle field is indeed the light from the source randomly remapped in space by the large number of scatterers in the turbid medium. Although often considered as noise, early experiments in holographic phase conjugation [12] have shown that the speckle field formed by a static medium does carry information about the source of the light. Retrieval of the source information can be achieved by sending a time-reversal replica back into the same medium where the scattering is precisely undone. The recent digital implementations of wavefront shaping [13] and holographic phase conjugation [14,15] using a spatial light modulator (SLM) show great promise in creating a light focus inside or through scattering media.

In the last few decades, many techniques have been developed for imaging inside or through turbid media. A relatively straightforward approach is to simply ignore the scattering since features larger than the thickness of the media are not lost due to the scattering. This led to the successful technique of diffusive optical tomography, which achieved molecular imaging in small animals with a resolution of

the order of ~millimeters using NIR illumination [16–18]. Optical mammography in humans [19–21] is also based on the same principle. Several methods, such as optical coherence tomography (OCT) [22], confocal [23], and two-photon microscopy [24], selectively collect directly transmitted, or ballistic light, and reject multiply scattered waves to achieve higher image quality. Selection of ballistic light can also be achieved through optical [25,26] or electronic [27,28] gating in the time domain. Deeper into the turbid medium, however, the ballistic light is extinguished exponentially by the scattering (due to Beer–Lambert law) and quickly becomes undetectable for any technique that relies on ballistic photons. For example, Theer and Denk suggested that the practical imaging depth limit of two-photon microscopy is approximately 7ℓ [29].

Due to the rapid attenuation of the ballistic light with depth, it is necessary to extract the scrambled information from the multiply scattered light. Central to this problem is the control of wave propagation in turbid media [4]. To achieve this, Popoff *et al.* [30] measured the monochromatic transmission matrix of a turbid medium, which allows focusing and imaging through the scattering medium. Time-resolved measurements of the scattered fluorescence intensity was used to retrieve the source image [31]. In another approach, ultrasound was used in combination with optical means in a variety of techniques [32–35] to exploit the relatively lower scattering in the acoustic domain. Furthermore, Vellekoop and Mosk [13] demonstrated an iterative method to find the optimal phase modulation (wavefront shaping) such that a premodulated light beam propagating back through the turbid medium achieves focus at a given point. A very tight focus was achieved using this technique [36]. Closely related to the wavefront shaping technique, digital holographic phase conjugation was also reported to achieve focusing through turbid media [14,15]. Both methods achieve imaging similarly by raster-scanning the focus through memory effect [10,11].

3. SHG as a Contrast Mechanism

When a scattering medium is illuminated, the large number of scatterers produce an overwhelming scattered light intensity such that any probes of a biologically relevant size (often of submicrometer or nanometer scale) cannot be detected using its own elastic scattering. Indeed, all techniques but OCT for imaging through turbid media require a type of optical beacon that converts the frequency of the illumination light into another, such that the background scattering can be efficiently suppressed using a simple optical filter. Fluorescent beacons are the key component for molecular specificity in fluorescence microscopy [37–39]. As a coherent beacon, SHG nanoprobes provide a unique opportunity for imaging through turbid media based on holographic phase conjugation.

When an optical medium is exposed to an intense light field $\mathbf{E}(\omega)$, the polarization density of the material is no longer linear to $\mathbf{E}(\omega)$. Rather, it has to be modeled as a Taylor expansion as $\mathbf{P} = \chi^{(1)} \cdot \mathbf{E}(\omega) + \chi^{(2)} \cdot \mathbf{E}^2(\omega) + \chi^{(3)} \cdot \mathbf{E}^3(\omega) + \ldots$, where the coefficient $\chi^{(n)}$ is the nth-order susceptibility of the material. The second-order response, $\chi^{(2)} \cdot \mathbf{E}^2(\omega)$, gives rise to a radiation at exactly twice the frequency of the applied field, a phenomenon known as SHG [40]. Figure 2(a) depicts the energy diagram of an SHG process, where a pair of fundamental photons is simultaneously annihilated while a single photon is emitted with exactly twice as much energy as each of the photons in the photon pair. Note that the electron that annihilates the photon pair only goes through a brief (a few femtoseconds) "virtual" energy state before returning to the ground state, and the energy is conserved in the entire process. Furthermore, in the SHG process, the second-harmonic radiation retains a deterministic phase relationship to the fundamental field and is therefore a coherent wave.

As illustrated in Fig. 2(b), SHG is only possible when symmetry is broken. The symmetry is broken at interfaces and SHG can occur there, but in the bulk it is efficient only in materials with noncentrosymmetric crystalline structures. Most turbid media, including a majority of biological materials, are unstructured and isotropic and are highly inefficient in SHG if possible at all. Therefore, SHG nanocrystals as reporter probes form a sharp contrast to the background emissions from the surrounding materials. They hence satisfy the requirement for a coherent light beacon. The SHG nanocrystals also have a

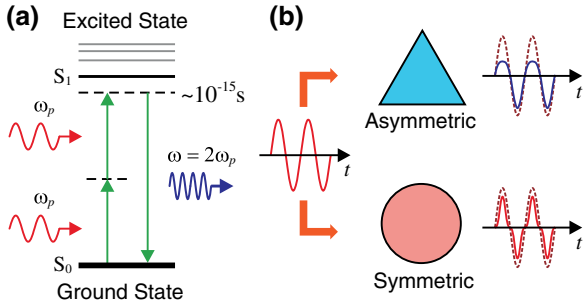

Fig. 2. (Color online) Principle of SHG. (a) Energy diagram for SHG. Two input photons are annihilated and one output photon of doubled frequency is produced simultaneously. The energy of the input photon pair is less than the lowest bandgap (S_1). The bond electrons undergo only a brief (a few femtoseconds) virtual transition before they emit a single photon with exactly doubled frequency and transit back to the ground state (S_0). Energy is conserved throughout the process. (b) Symmetry selectivity in the SHG process. When illuminated by an intense light beam, the polarization response of materials with different symmetry deviates from the input (fundamental) differently. An asymmetric system (blue triangle) produces an asymmetric deviation (blue solid curve), leading to SHG radiation and possibly higher even-order harmonics. A symmetric system (red circle) produces a symmetric deviation (red solid curve) where all even-order harmonics cancels out, permitting only odd-order harmonics. The dark red dotted curves indicate linear polarization response.

number of other highly desired properties as probes for biomedical imaging applications, such as resistance against photobleaching and steady emissions [41,42].

4. Materials for SHG Microscopy

Developing nanomaterials suitable for SHG probes plays a central role in the field of SHG imaging. From the perspective of applications in biomedical imaging, materials for SHG probes can be roughly categorized as endogenous and exogenous. Endogenous materials include those biological tissues that have ordered structures with no inversion symmetry. Exogenous materials comprise organic dyes or crystals, metal nanostructures, and dielectric or semiconductor nanoparticles, whose atom arrangements lack an inversion center. While endogenous SHG offers a great advantage of label-free structural imaging, molecular-specific probing can be only achieved through externally introduced SHG agents.

In one of the pioneering works, Campagnola *et al.* [43] demonstrated SHG microscopy in a variety of samples, covering connective tissues, muscle tissues, and intracellular microtubules. Zoumi *et al.* [44] and Zipfel *et al.* [45] investigated SHG imaging in collagen fibers, a highly efficient intercellular tissue for SHG. Plotnikov *et al.* [46] studied SHG in myosin of muscle sarcomeres in more detail. Second-harmonic emission was also reported in myelinated nerve fibers [47] and brain tissues [48]. Moreover, the green fluorescent protein was found to be SHG-active [49,50]. Applications of the native SHG from collagen in cancer diagnostics were also reported [51,52]. Due to the phase matching condition, endogenous SHG microscopy commonly utilizes transmission-side detection, although it was shown that echo-planar imaging detection is feasible and advantageous when tissue turbidity is high [53]. Since laser-scanning microscopy with the native SHG emission requires little change in the existing multiphoton microscopes, it can be conveniently integrated into fluorescence microscopy to provide multimodal imaging capabilities [44,45,53,54].

Organic molecules and polymers containing π-bonds and a permanent electric dipole moment that breaks the symmetry demonstrate second-order nonlinearities. Para-nitoaniline and a variety of stilbene derivatives are among the typical molecules investigated in early works [55,56]. Delocalized π-electrons, which can move freely along the conjugated structure of the molecules and polymers, play a crucial role to the high nonlinearities in organic materials. Because of the small size of the molecules compared with most inorganic SHG nanocrystals of comparable response, molecular SHG chromophores are of great interest for biomedical applications. Design and synthesis of such chromophores have become an area of intense effort [57–62]. In particular, many organometallic complexes show excellent SHG capability [59,60,62]. Furthermore, a unique on-off switchable SHG response has been recently demonstrated in certain organometallic compounds [63], which is not available in other types of SHG materials and may play a key role in an SHG variant of stochastic optical reconstruction microscopy [64,65]. Organic SHG chromophores have been used in the imaging of cell membranes [66,67] and neural signals [68,69].

Interfaces break the symmetry and are therefore capable of SHG [70]. Due to the large ratio of surface area to volume, nanometer-scale structures generate SHG radiation even though the underlying atom arrangement and the shape are centrosymmetric. Dadap *et al.* [71] gave a theoretical treatment to this problem in the Rayleigh limit and suggested that the SHG radiation as such is quadrupolar in the leading term. The theory and its later expansion [72], as well as works by others [73], also predicts that dipole radiation is possible under tightly focused (nonlocal) excitation. Because of their large polarizability, metal nanoparticles (particularly of Au and Ag) are of intense interest for practical use as SHG light sources, with a wealth of works in theory [74–77] and experiments [78–81]. In particular, the highly desirable enhancement of SHG through plasmonic resonance [82] is often achievable in noble metal nanoparticles. Furthermore, SHG emission can also be enhanced through the introduction of geometric asymmetry [83,84], chirality [85,86], or more complex structures [87]. Due to the nature of a surface effect, nanometer SHG emitters constructed from centrosymmetric materials are generally inefficient for practical far-field imaging of single particles below 100 nm in size. Indeed, SHG imaging of individual 150 nm gold nanoparticles was demonstrated only recently using a fairly high excitation intensity (5×10^{11} W cm^{-2}) and a long integration time (10 s/pixel) in the detection [81].

Noncentrosymmetric nanocrystals of inorganic materials are often efficient SHG emitters since the asymmetric arrangement of atoms allows the entire volume to contribute to the SHG radiation. Wide bandgap materials are generally preferred for minimal optical absorption and the associated photodamage and phototoxicity. A variety of wide bandgap materials has been investigated, including ZnO [88–91], $LiNbO_3$ [92,93], $KNbO_3$ [93–95], $KTiOPO_4$ [41,96], $BaTiO_3$ [42,90,97,98], and $Fe(IO_3)_3$ [99]. In terms of biomedical applications, SHG microscopy in cells and tissues using these nonlinear optical probes has been reported [42,100–102]. Staedler *et al.* [103] investigated the biocompatibility of a range of nanocrystals and suggested that $BaTiO_3$ is the most biocompatible among the materials investigated. Hsieh *et al.* [104] developed a chemical scheme for molecular-specific bioconjugation of antibodies to $BaTiO_3$ nanocrystals. Nonlinear correlation spectroscopy using ensembles of the SHG nanocrystals was also reported [105]. Compared with wide bandgap materials, semiconductor nanocrystals of II-VI and III-V family materials often provide much stronger SHG response and achieve smaller particle size, which is a highly sought-after property in biomedical

applications. These include CdSe [106], CdS [107], CdTe [108,109], GaAs [110], and InP [111], among others. The overall photon energy is no longer conserved in this case, since a significant amount of the energy is consumed through two-photon absorption and fluorescence. The SHG signal in these materials is therefore usually accompanied by a strong two-photon excited fluorescence emission [106].

In an SHG nanoprobe (assumed spherical) that is much smaller than the wavelength of the harmonic, dipole radiation dominates. The radiated power in the doubled frequency given a fundamental intensity I is $W^{(2\omega)} = \sigma^{(2\omega)} I^2$, where $\sigma^{(2\omega)} \propto d^2 a^6$ is the SHG scattering cross section and a is the radius of the sphere. Analogous to the two-photon fluorescence action cross section, $\sigma^{(2\omega)}$ is also measured in the Göppert-Mayer (GM) unit with $1\ \mathrm{GM} = 10^{-50}\ \mathrm{cm}^4\,\mathrm{s\,photon}^{-1}$. The sixth-order dependency of the radiation power on the particle size causes a severe sensitivity problem in practice when the particle is scaled down below 100 nm. Furthermore, if an SHG beacon is to be placed behind a turbid media, the lowered fundamental intensity and the loss of the SHG radiation (both due to the scattering) call for highly sensitive nanoprobes. To boost the second-harmonic radiation power in free-standing nanoprobes, Pu *et al.* [112] synthesized plasmonic core-shell nanocavities containing an SHG nanoparticle core [Fig. 3(a)]. The highly concentrated local field at resonance results in drastically enhanced SHG emission despite the transmission loss in the plasmonic shell. As shown in Fig. 3(b), the measured resonant SHG enhancement factor exceeded 500.

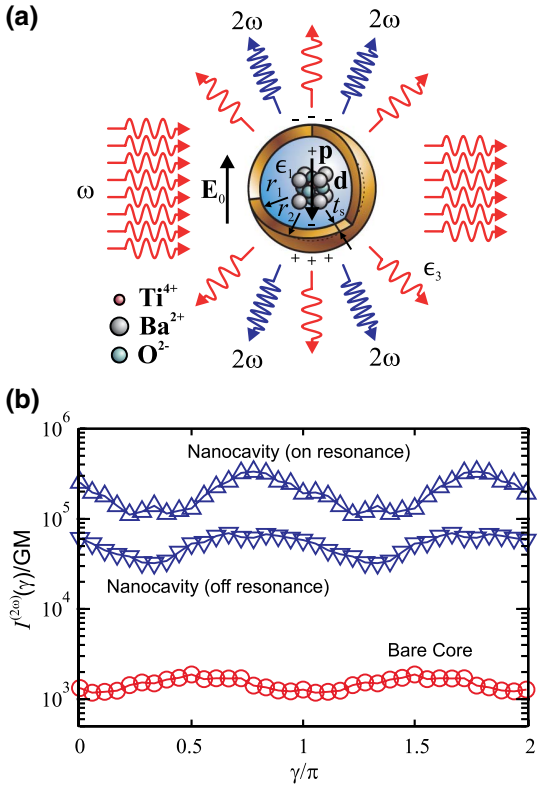

Fig. 3. (Color online) Enhancement of SHG in a resonating plasmonic core-shell nanocavity. (a) Principle of the SHG enhancement. In a plasmonic nanocavity encaging an SHG nanocrystal, resonantly driven by an external optical field $\mathbf{E}_0$ at the fundamental frequency ω, the internal electric field is enhanced, leading to significantly stronger SHG radiation. (b) Experimental measurements for the SHG scattering cross section (in unit of GM) of a bare core particle (red circles), an on-resonance nanocavity (blue up triangles), and an off-resonance nanocavity (blue down triangles). All measurements are a function of the fundamental polarization angle. The resonant SHG enhancement factor of the nanocavity over a bare core particle is greater than 500. Adapted from [112].

5. Harmonic Holography

The principle of H^2 [5] is an extension of the traditional holographic principle through nonlinear optics. Based on the coherent nature of the SHG process, holographic imaging was achieved through the interference between the second-harmonic waves independently generated by physically separated nonlinear optical crystals. One of the goals of H^2 is to introduce a contrast forming mechanism into holography while maintain its capability of three-dimensional (3D) imaging. Figure 4 illustrates the principle of H^2, where a cube, a cone, and a sphere are used as the objects of concern, among which we assume only the sphere is of our interest. In conventional holography [Fig. 4(a)], all objects scatter in the same optical frequency as the reference and are thus later reconstructed indiscriminately. In H^2 [Fig. 4(b)], on the other hand, the objects are illuminated by the fundamental light and only the object of interest (the sphere) is marked with SHG materials and thus scatters an SHG wave. The SHG reference, independently generated using a separate nonlinear optical crystal, interferes with the signal wave on the image sensor after a bandpass filter that rejects the fundamental light, and forms a hologram. The reconstructed image from a hologram as such contains only the object of interest (the sphere). This new holographic principle thus provides a mechanism to create a contrast between the objects of interest and the rest.

The proof-of-principle experiment for H^2 was first demonstrated in 2008 by Pu *et al.* [5] using large (~10 μm) clusters of 100 nm $BaTiO_3$ nanocrystals and an amplified Ti:sapphire laser source giving an excitation intensity of $1 \times 10^{11}\ \mathrm{W/cm}^2$. Owing to the powerful laser source, single-shot H^2 recording was achieved. Hsieh *et al.* later used a similar setup [Fig. 5(a)] to image 3D distribution of 100 nm $BaTiO_3$ nanoprobes adsorbed to the membrane of HeLa cells. In the context of biomedical imaging, the SHG nanoprobes are often called second-harmonic radiation imaging probes (SHRIMPs). Figures 5(b)–5(e) show the reconstructed images of selected planes from a volumetric image stack, and the axial intensity profile at selected location is plotted in Fig. 5(f). The high contrast against the background and the 3D capability of the harmonic holographic microscopy is clearly demonstrated. More details on the topic of H^2 can be found in [113].

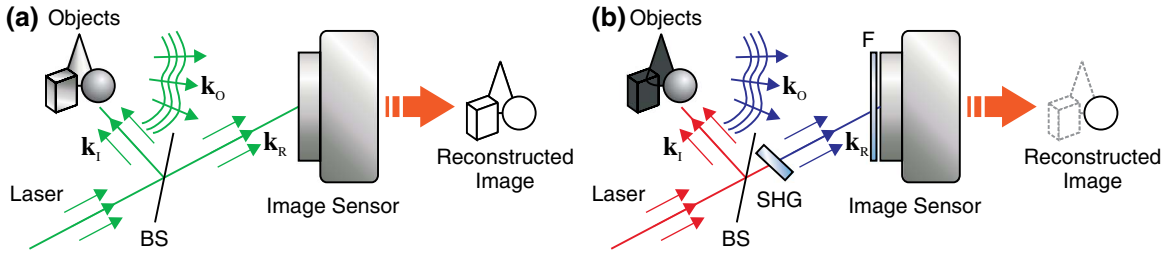

Fig. 4. (Color online) Principle of H^2. (a) In a conventional holography, the objects (represented by a cube, a cone, and a sphere) scatter at the same frequency with the illumination and the reference light (marked in green). The image sensor records the fringes formed by the interference between the scattered light from the object and the reference light. Through numerical reconstruction, a 3D image of all objects (represented in black solid shape outlines) is retrieved. (b) In H^2, the object of interest (the sphere as an example) is tagged with nonlinear optical material that is capable of generating optical harmonics (for example SHG). When excited by the illumination light (marked in red), only the sphere scatters light at the doubled frequency that can pass the bandpass filter F. The linearly scattered waves (not shown for clarity) at the same frequency with the illumination light are rejected by the filter. The reference wave goes through an independent nonlinear optical crystal for frequency conversion before reaching the image sensor. The image sensor therefore records a hologram that only contains the wave from the sphere. The numerical reconstruction is able to retrieve only the sphere (black solid shape) but reject the cube and the cone (gray dashed shapes). $\mathbf{k}_I$, $\mathbf{k}_O$, and $\mathbf{k}_R$: the wave vectors of the illumination, object, and reference waves, respectively. BS, beam splitter.

Recently, H^2 has also been applied to microscopy using the endogenous SHG signal from biological samples. Masihzadeh *et al.* [114] achieved 3D imaging in samples of corn seeds and human muscle fibrils using a Yb:KGW femtosecond oscillator at a fundamental wavelength of 1027 nm. An SNR of 25 dB was obtained in an integration time as short as 10 ms with an electron-multiplying charge-coupled device (CCD). Winters *et al.* [115] devised a technique to extract rich information on the supramolecular organization from polarization-resolved harmonic holographic microscopy in samples of corn seed and canine tongue. Shaffer *et al.* [116] obtained single-shot SHG phase image in a sample of mouse tail tendon using a Ti:sapphire oscillator working at 800 nm. Furthermore, the principle of H^2 is not limited to SHG but also applies to any coherent nonlinear optical process, such as third-harmonic generation and coherent anti-Stokes Raman scattering (CARS). For example, Shi *et al.* [117] demonstrated an experiment of holographic recording using CARS signal for chemically selective imaging, which has recently been applied to cell imaging [118].

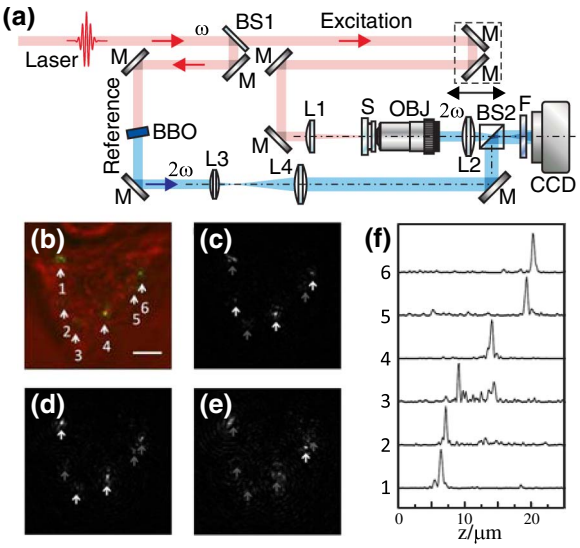

Fig. 5. (Color online) 3D imaging in cells with H^2. (a) Experimental setup for 3D imaging of SHRIMPs in cells using H^2. (b) Simultaneous transmission microscopy of a HeLa cell (red channel) and SHG images of six SHRIMP clusters (green channel) adsorbed on its membrane. SHRIMPs found in the viewing field are labeled 1–6. Note that not all SHRIMPs are in focus due to their 3D distribution. (c)–(e) numerically reconstructed images at selected planes from an image stack. The distance between the adjacent planes is approximately 3 μm. The white arrows indicate the on-focus images of SHRIMPs, while the gray arrows indicate the out-of-focus images of SHRIMPs. (f) Normalized axial intensity profiles of the six clusters. The scale bar is 5 μm. (b)–(f) reproduced from [98].

6. Imaging through Turbid Media with H^2

Coherent SHG beacons enable imaging through turbid media with H^2. Earlier experiments [12,14] have shown that holographic phase conjugation achieves focusing of light through a turbid medium but lacks a contrast mechanism to distinguish the useful signal from the background scattering. Harmonic holography and SHG beacons (SHRIMPs) provide the required contrast. The principle of imaging through a turbid medium using H^2 phase conjugation is illustrated in Fig. 6. Two major steps (see below) are involved: focusing through phase conjugation [Fig. 6(a)] and scanning via memory effect [Figs. 6(b) and 6(c)].

In the first step, the SHRIMP beacon S is excited by the illumination light and radiates a light field E_O at the doubled frequency, which becomes a speckle field E_S after going through the scattering medium. Using H^2, the complex amplitude of E_S is recorded, whose conjugate E_S^* is recreated and sent back through the medium. The scatterers in the turbid medium, which is assumed to be static during the process, cancel the scattering effect and restore a wavefront E_O^* that focuses at the position of the SHRIMP. For simplicity, the excitation light is shown

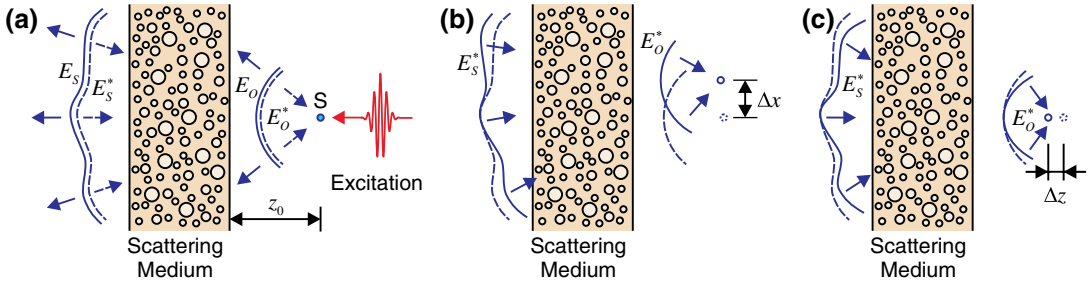

Fig. 6. (Color online) Principle of imaging through turbid media with harmonic holographic phase conjugation. (a) To achieve focusing through the turbid medium, a SHRIMP (blue filled solid circle) is used as a light beacon and radiates frequency-doubled light under the excitation of an intense short laser pulse. The optical field E_O (blue solid curve to the left of the medium) generated by the SHRIMP undergoes multiple scattering while transmitting through the scattering medium and becomes the scattered field E_S (blue solid curve to the right of the medium). Through harmonic holographic phase conjugation, the conjugated wavefront E_S^* in the doubled frequency is reestablished. After transmitting back through the original scattering medium, all scattering distortions are canceled and the conjugated wavefront E_O^* (blue dashed curve to the right of the medium) is reconstructed, which forms a focus at the original position of the SHRIMP. (b) Lateral scanning can be achieved through the transverse memory effect in the disordered medium. When the phase-conjugated wave field (blue dashed curve) is rotated by an angle before being sent back through the original medium, the focus (blue open solid circle) is transversely displaced by Δx from the original SHRIMP position (blue open dashed circle) albeit with a lower intensity. This enables the scanning in the transverse dimension by a controlled rotation angle. (c) Axial scanning can be achieved through the axial memory effect in the disordered medium. When the phase-conjugated wave field (blue dashed curve) is bent by a curvature before being sent back through the original medium, the focus (blue open solid circle) is axially displaced by Δz from the original SHRIMP position (blue open dashed circle) with a lower intensity. This enables the scanning in the axial dimension by a controlled curvature.

from the right side of the turbid medium. In real applications, the excitation light is sent from the same side as the detection despite the lowered intensity and spoiled spatiotemporal profile at the beacon position, since the other side is generally inaccessible.

In the second step, scanning in the vicinity of the SHRIMP beacon is achieved through proper manipulations of the phase-conjugated wavefront. Previous studies [10,11] in the multiple scattering of coherent waves in disordered media have revealed a deterministic intensity-intensity correlation in the wave exiting the medium when the incident wave undergoes a small change. Therefore, rotating the incident wavefront by a small angle θ moves the phase conjugated focus laterally by $\Delta x = (L + z_0)\theta$ [Fig. 6(b)]. Similarly, if the incident wavefront is bent by a curvature $1/R$, the restored focus is axially shifted by $\Delta z = (L + z_0)^2/(R - L - z_0)$. The displacement calculation is based on the assumption that the wave is pivoted and tangent on the incident face of the medium for the rotation and bending, respectively.

Hsieh *et al.* [15] demonstrated efficient focusing of light through a turbid medium using H^2 phase conjugation. Their experimental setup is illustrated in Figs. 7(a) and 7(b) for recording and reconstruction, respectively. Components not directly involved in the operation are shown in gray outlines in the figure. The system first record the phase of the SHG light field emitted from the SHRIMP and scattered by a turbid layer [Fig. 7(c)]. Next, a light field with the conjugated phase is created by the SLM and sent back through the turbid layer along the same path. The scattering of the turbid layer is canceled by the conjugated phase, and a focus is reconstructed at the location of the SHRIMP. Without the phase conjugation, the light field in the vicinity area of the SHRIMP is simply a speckle pattern [Fig. 7(d)]. Through the phase conjugation, a clear focus is recovered [Fig. 7(e)], whose intensity line profile [Fig. 7(f)] shows nearly diffraction-limited performance.

In order to apply the H^2 phase conjugation technique to imaging, scanning of the conjugated focus through memory effect was later demonstrated by Hsieh *et al.* [119]. The experimental setup involves a galvo mirror for controlled angular rotation, and CCD2 was replaced by a photomultiplier (PMT). The target was a photolithographic pattern of gold on a glass plate, as seen in Fig. 7(g). A SHRIMP beacon was placed in the center of the pattern for H^2 recording, and a ground glass diffuser was used as a turbid layer. Scanning the phase-conjugated focus over the target and collecting the transmitted light with the PMT recreated the target pattern [Fig. 7(h)] with good SNR and contrast. In the control experiment without phase conjugation, no pattern was reconstructed (data not shown).

Yang *et al.* [120] showed for the first time with experiments the scanning of the phase-conjugated focus in the axial dimension. They employed a similar arrangement with the previous experiments, as shown in Figs. 7(a) and 7(b). The scanning, however, was implemented digitally using the SLM rather than a galvo mirror for scanning in both lateral and axial dimension. To demonstrate the ability of 3D imaging, a target was assembled by dispersing fluorescent beads on both sides of a microscope cover slip and SHRIMP beacons only on one side, as shown in Fig. 7(i). A few layers of scotch tape were used as the turbid layer. Once the phase conjugation was established, linear and quadratic phase shifts were applied to the phase map on the SLM to achieve transverse and axial scanning. The images of the fluorescent beads obtained on side 1 and 2 with

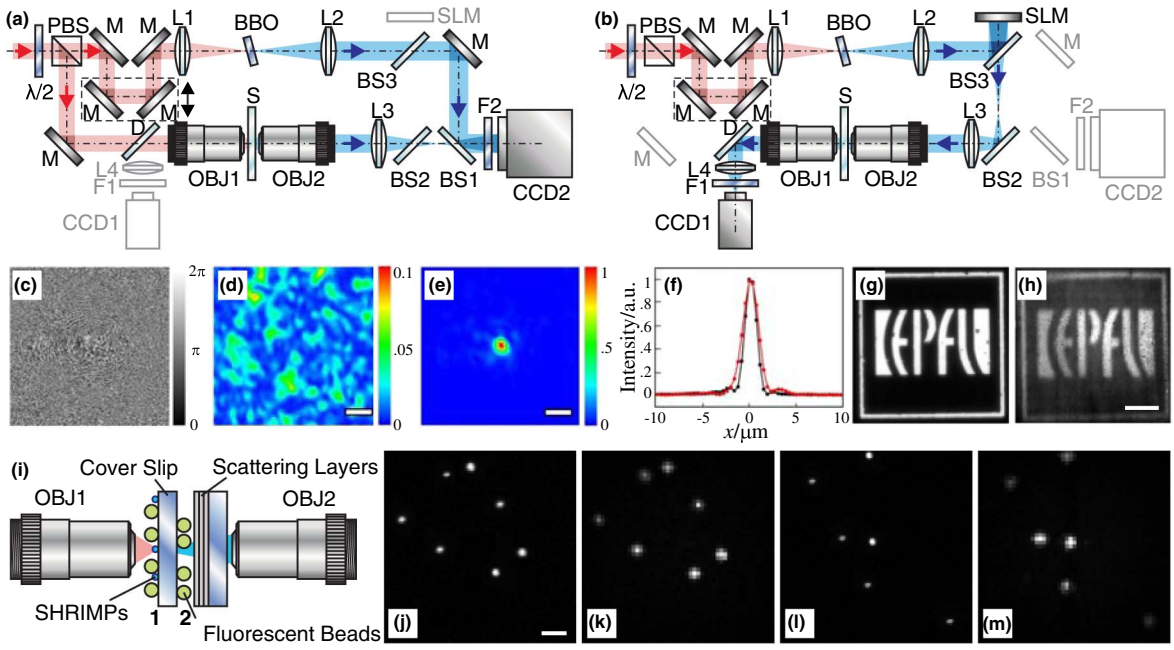

Fig. 7. (Color online) Experiments of phase conjugation and imaging through turbid media using H^2. (a) Experimental setup for H^2 recording of the scattered light field. The sample S contains isolated SHRIMPs behind (from the view of CCD2) a turbid layer. The digital camera CCD2 records the holograms formed by the scattered SHG light field and the second harmonic reference generated independently by a BBO. Parts outlined in gray are not involved in the recording process. (b) Digital phase conjugation. The second harmonic reference is directed to the SLM where the conjugated wavefront is recreated, goes through the same turbid layer, and focuses onto CCD1. Parts outlined in gray are not involved in the phase conjugation process. $\lambda/2$, half-wave plate; BBO, beta-barium borate; PBS, polarization beam splitter; M, mirror; D, dichroic mirror; L1–L4, lens; OBJ1 and OBJ2, microscope objectives; S, sample; BS1–BS3, beam splitters; F1 and F2, SHG bandpass filter. (c) Conjugated phase pattern of the scattered SHG field extracted from the hologram and projected onto the SLM. (d) Normalized intensity image of the highly distorted focus without phase conjugation. (e) Normalized intensity image (captured by CCD1) of the phase-conjugated focus through the turbid medium by using the phase pattern shown in (a). The scale bar is 5 μm in (d) and (e). (f) Comparison of the phase-conjugated focus with the diffraction limit. Red: normalized intensity profile of the phase-conjugated focus. Black: normalized intensity profile of the diffraction limited focus. The FWHMs of the phase-conjugated and diffraction limit are 2.30 and 1.95 μm, respectively. (g) Wide-field transmission image of the scanning target, a 130 nm thick gold pattern on a glass substrate prepared by photolithography. The bright region indicates the transparent area. (h) Phase-conjugate scanning image of the target. The target pattern is clearly resolved. The scale bar is 25 μm in (g) and (h). (i) Sample used in the experiment of 3D laser-scanning fluorescence imaging through turbid media. Fluorescent beads (2–5 μm) are randomly deposited on both sides of a cover slip as the imaging targets. Sparse SHRIMPs are dispersed on one side of the cover slip as beacons. The 3D imaging is achieved by scanning the phase conjugation focus in the vicinity volume and collecting the fluorescence signal. (j) and (k) Direct (without the turbid layers) wide-field microscopy and the phase-conjugated scanning image (through the turbid layers) on side 1, respectively. (l) and (m) Direct wide-field microscopy and the phase-conjugated scanning image on side 2, respectively. The scale bar is 10 μm in (j)–(m). (c)–(f) reproduced from [15], (g) and (h) reproduced from [119], (j)–(m) reproduced from [120].

direct microscopy without the presence of the turbid layers are displayed in Figs. 7(j) and 7(l). The corresponding scanned images through the turbid layer are shown in Figs. 7(k) and 7(m). A clear correspondence between the images of the fluorescent beads is found between the direct and the scanned images.

It is interesting to compare the techniques of wavefront shaping [13] and H^2 phase conjugation. The focusing performance should be similar, though H^2 phase conjugation as a high-resolution equivalent to wavefront shaping may result in slightly tighter focus. Wavefront shaping requires many measurements in order to figure out an optimum phase map, while H^2 phase conjugation only needs to measure once. Thus, the latter suits a dynamic system better. The cost, however, is the alignment condition: in a thick scattering medium the phase conjugation wavefront needs to be aligned in all six degrees of freedom in order to obtain efficient cancelation of the scattering. Wavefront shaping, on the other hand, does not require an alignment procedure. Facing a situation of multiple beacons, wavefront shaping is more likely to fail since the detected fluorescence signal is an intermingled emission at different phases. H^2 phase conjugation, on the other hand, still achieves a focus at each beacon position, although scanning becomes difficult. Being a two-photon process, H^2 phase conjugation inherently requires pulsed illumination light with high intensity. Thus, the scattering makes it difficult to perform the illumination and H^2 recording from the same side. However, with more sensitive SHG nanoprobes, such as SHG plasmonic nanocavities [112], same-side imaging is feasible, making H^2 phase conjugation a highly useful technique for deep tissue imaging.

7. Summary

The interest in seeing through an opaque biological boy optically is rapidly growing and attracts intense research efforts. The opacity in the red and near-infrared spectral region is dominated by scattering in most biological tissues, where information is scrambled rather than lost in the process of scattering. This provides an opportunity for reconstructing the image from the scattered light. Over the past decade many techniques have been developed to accomplish this goal, and holographic phase conjugation is among the earliest and most efficient methods. Through holographic phase conjugation, a focus can be restored through the scattering media if a light beacon is first established at the location of the focus. Once created, the focus can be moved for scanning microscopy through the memory effect by manipulating the phase of the phase-conjugated wavefront. Harmonic holography further introduces a unique nonlinear optical contrast-forming mechanism, namely SHG, to efficiently suppress the overwhelming elastic scattering due to the turbidity while maintaining the capability of holographic wavefront reconstruction. Both two-dimensional and three-dimensional scanning microscopy through turbid media has been demonstrated through harmonic holographic phase conjugation. The recent advent of highly sensitive SHG nanoprobes could enable same-side illumination and recording, which will make this technique highly useful in the field of biomedical imaging.

References

1. D. J. Brenner and E. J. Hall, "Computed tomography—An increasing source of radiation exposure," N. Engl. J. Med. **357**, 2277–2284 (2007).
2. S. R. Arridge, "Optical tomography in medical imaging," Inverse Probl. **15**, R41–R93 (1999).
3. C. Haisch, "Optical tomography," Annu. Rev. Anal. Chem. **5**, 57–77 (2012).
4. A. P. Mosk, A. Lagendijk, G. Lerosey, and M. Fink, "Controlling waves in space and time for imaging and focusing in complex media," Nat. Photonics **6**, 283–292 (2012).
5. Y. Pu, M. Centurion, and D. Psaltis, "Harmonic holography: a new holographic principle," Appl. Opt. **47**, A103–A110 (2008).
6. M. C. W. van Rossum and T. M. Nieuwenhuizen, "Multiple scattering of classical waves: microscopy, mesoscopy, and diffusion," Rev. Mod. Phys. **71**, 313–371 (1999).
7. C. Balas, "Review of biomedical optical imaging-a powerful, non-invasive, non-ionizing technology for improving in vivo diagnosis," Meas. Sci. Technol. **20**, 104020 (2009).
8. P. W. Anderson, "Absence of diffusion in certain random lattices," Phys. Rev. **109**, 1492–1505 (1958).
9. L. V. Wang and H. Wu, *Biomedical Optics: Principles and Imaging* (Wiley, 2007).
10. S. C. Feng, C. Kane, P. A. Lee, and A. D. Stone, "Correlations and fluctuations of coherent wave transmission through disordered media," Phys. Rev. Lett. **61**, 834–837 (1988).
11. I. Freund, M. Rosenbluh, and S. Feng, "Memory effects in propagation of optical waves through disordered media," Phys. Rev. Lett. **61**, 2328–2331 (1988).
12. E. N. Leith and J. Upatniek, "Holographic imagery through diffusing media," J. Opt. Soc. Am. **56**, 523–523 (1966).
13. I. M. Vellekoop and A. P. Mosk, "Focusing coherent light through opaque strongly scattering media," Opt. Lett. **32**, 2309–2311 (2007).
14. M. Cui and C. H. Yang, "Implementation of a digital optical phase conjugation system and its application to study the robustness of turbidity suppression by phase conjugation," Opt. Express **18**, 3444–3455 (2010).
15. C. L. Hsieh, Y. Pu, R. Grange, and D. Psaltis, "Digital phase conjugation of second harmonic radiation emitted by nanoparticles in turbid media," Opt. Express **18**, 12283–12290 (2010).
16. V. Ntziachristos, C. Bremer, and R. Weissleder, "Fluorescence imaging with near-infrared light: new technological advances that enable in vivo molecular imaging," Eur. Radiol. **13**, 195–208 (2003).
17. T. F. Massoud and S. S. Gambhir, "Molecular imaging in living subjects: seeing fundamental biological processes in a new light," Genes Dev. **17**, 545–580 (2003).
18. R. Weissleder, "Scaling down imaging: molecular mapping of cancer in mice," Nat. Rev. Cancer **2**, 11–18 (2002).
19. S. B. Colak, M. B. van der Mark, G. W. Hooft, J. H. Hoogenraad, E. S. van der Linden, and F. A. Kuijpers, "Clinical optical tomography and NIR spectroscopy for breast cancer detection," IEEE J. Sel. Top. Quantum Electron. **5**, 1143–1158 (1999).
20. R. Choe, A. Corlu, K. Lee, T. Durduran, S. D. Konecky, M. Grosicka-Koptyra, S. R. Arridge, B. J. Czerniecki, D. L. Fraker, A. DeMichele, B. Chance, M. A. Rosen, and A. G. Yodh, "Diffuse optical tomography of breast cancer during neoadjuvant chemotherapy: a case study with comparison to MRI," Med. Phys. **32**, 1128–1139 (2005).
21. A. Corlu, R. Choe, T. Durduran, M. A. Rosen, M. Schweiger, S. R. Arridge, M. D. Schnall, and A. G. Yodh, "Three-dimensional in vivo fluorescence diffuse optical tomography of breast cancer in humans," Opt. Express **15**, 6696–6716 (2007).
22. D. Huang, E. A. Swanson, C. P. Lin, J. S. Schuman, W. G. Stinson, W. Chang, M. R. Hee, T. Flotte, K. Gregory, C. A. Puliafito, and J. G. Fujimoto, "Optical coherence tomography," Science **254**, 1178–1181 (1991).
23. J. M. Schmitt, A. Knuttel, and M. Yadlowsky, "Confocal microscopy in turbid media," J. Opt. Soc. Am. A **11**, 2226–2235 (1994).
24. F. Helmchen and W. Denk, "Deep tissue two-photon microscopy," Nat. Methods **2**, 932–940 (2005).
25. L. Wang, P. P. Ho, C. Liu, G. Zhang, and R. R. Alfano, "Ballistic 2-D imaging through scattering walls using an ultrafast optical Kerr gate," Science **253**, 769–771 (1991).
26. A. Bassi, D. Brida, C. D'Andrea, G. Valentini, R. Cubeddu, S. De Silvestri, and G. Cerullo, "Time-gated optical projection tomography," Opt. Lett. **35**, 2732–2734 (2010).
27. M. J. Niedre, R. H. de Kleine, E. Aikawa, D. G. Kirsch, R. Weissleder, and V. Ntziachristos, "Early photon tomography allows fluorescence detection of lung carcinomas and disease progression in mice in vivo," Proc. Natl. Acad. Sci. USA **105**, 19126–19131 (2008).
28. B. Zhang, X. Cao, F. Liu, X. Liu, X. Wang, and J. Bai, "Early-photon fluorescence tomography of a heterogeneous mouse model with the telegraph equation," Appl. Opt. **50**, 5397–5407 (2011).
29. P. Theer and W. Denk, "On the fundamental imaging-depth limit in two-photon microscopy," J. Opt. Soc. Am. A **23**, 3139–3149 (2006).
30. S. M. Popoff, G. Lerosey, R. Carminati, M. Fink, A. C. Boccara, and S. Gigan, "Measuring the transmission matrix in optics: an approach to the study and control of light propagation in disordered media," Phys. Rev. Lett. **104**, 100601 (2010).
31. V. Venugopal, J. Chen, F. Lesage, and X. Intes, "Full-field time-resolved fluorescence tomography of small animals," Opt. Lett. **35**, 3189–3191 (2010).
32. M. Kempe, M. Larionov, D. Zaslavsky, and A. Z. Genack, "Acousto-optic tomography with multiply scattered light," J. Opt. Soc. Am. A **14**, 1151–1158 (1997).
33. B. H. Yuan, S. Uchiyama, Y. Liu, K. T. Nguyen, and G. Alexandrakis, "High-resolution imaging in a deep turbid medium based on an ultrasound-switchable fluorescence technique," Appl. Phys. Lett. **101**, 033703 (2012).
34. J. Gamelin, A. Aguirre, A. Maurudis, F. Huang, D. Castillo, L. V. Wang, and Q. Zhu, "Curved array photoacoustic

tomographic system for small animal imaging," J. Biomed. Opt. **13**, 024007 (2008).
35. Y. T. Lin, L. Bolisay, M. Ghijsen, T. C. Kwong, and G. Gulsen, "Temperature-modulated fluorescence tomography in a turbid media," Appl. Phys. Lett. **100**, 073702 (2012).
36. E. G. van Putten, D. Akbulut, J. Bertolotti, W. L. Vos, A. Lagendijk, and A. P. Mosk, "Scattering lens resolves sub-100 nm structures with visible light," Phys. Rev. Lett. **106**, 193905 (2011).
37. X. H. Gao, L. L. Yang, J. A. Petros, F. F. Marshal, J. W. Simons, and S. M. Nie, "In vivo molecular and cellular imaging with quantum dots," Curr. Opin. Biotechnol. **16**, 63–72 (2005).
38. B. N. G. Giepmans, S. R. Adams, M. H. Ellisman, and R. Y. Tsien, "The fluorescent toolbox for assessing protein location and function," Science **312**, 217–224 (2006).
39. S. Weiss, "Fluorescence spectroscopy of single biomolecules," Science **283**, 1676–1683 (1999).
40. P. A. Franken, G. Weinreich, C. W. Peters, and A. E. Hill, "Generation of optical harmonics," Phys. Rev. Lett. **7**, 118–119 (1961).
41. L. Le Xuan, C. Zhou, A. Slablab, D. Chauvat, C. Tard, S. Perruchas, T. Gacoin, P. Villeval, and J. F. Roch, "Photostable second-harmonic generation from a single $KTiOPO_4$ nanocrystal for nonlinear microscopy," Small **4**, 1332–1336 (2008).
42. P. Pantazis, J. Maloney, D. Wu, and S. E. Fraser, "Second harmonic generating (SHG) nanoprobes for in vivo imaging," Proc. Natl. Acad. Sci. USA **107**, 14535–14540 (2010).
43. P. J. Campagnola, A. C. Millard, M. Terasaki, P. E. Hoppe, C. J. Malone, and W. A. Mohler, "Three-dimensional high-resolution second-harmonic generation imaging of endogenous structural proteins in biological tissues," Biophys. J. **82**, 493–508 (2002).
44. A. Zoumi, A. Yeh, and B. J. Tromberg, "Imaging cells and extracellular matrix in vivo by using second-harmonic generation and two-photon excited fluorescence," Proc. Natl. Acad. Sci. USA **99**, 11014–11019 (2002).
45. W. R. Zipfel, R. M. Williams, R. Christie, A. Y. Nikitin, B. T. Hyman, and W. W. Webb, "Live tissue intrinsic emission microscopy using multiphoton-excited native fluorescence and second harmonic generation," Proc. Natl. Acad. Sci. USA **100**, 7075–7080 (2003).
46. S. V. Plotnikov, A. C. Millard, P. J. Campagnola, and W. A. Mohler, "Characterization of the myosin-based source for second-harmonic generation from muscle sarcomeres," Biophys. J. **90**, 693–703 (2006).
47. S. Y. Chen, C. S. Hsieh, S. W. Chu, C. Y. Lin, C. Y. Ko, Y. C. Chen, H. J. Tsai, C. H. Hu, and C. K. Sun, "Noninvasive harmonics optical microscopy for long-term observation of embryonic nervous system development in vivo," J. Biomed. Opt. **11**, 054022 (2006).
48. D. A. Dombeck, K. A. Kasischke, H. D. Vishwasrao, M. Ingelsson, B. T. Hyman, and W. W. Webb, "Uniform polarity microtubule assemblies imaged in native brain tissue by second-harmonic generation microscopy," Proc. Natl. Acad. Sci. USA **100**, 7081–7086 (2003).
49. A. Khatchatouriants, A. Lewis, Z. Rothman, L. Loew, and M. Treinin, "GFP is a selective non-linear optical sensor of electrophysiological processes in Caenorhabditis elegans," Biophys. J. **79**, 2345–2352 (2000).
50. I. Asselberghs, C. Flors, L. Ferrighi, E. Botek, B. Champagne, H. Mizuno, R. Ando, A. Miyawaki, J. Hofkens, M. Van der Auweraer, and K. Clays, "Second-harmonic generation in GFP-like proteins," J. Am. Chem. Soc. **130**, 15713–15719 (2008).
51. P. P. Provenzano, K. W. Eliceiri, J. M. Campbell, D. R. Inman, J. G. White, and P. J. Keely, "Collagen reorganization at the tumor-stromal interface facilitates local invasion," BMC Med. **4**, 38 (2006).
52. T. Stylianopoulos, B. Diop-Frimpong, L. L. Munn, and R. K. Jain, "Diffusion anisotropy in collagen gels and tumors: the effect of fiber network orientation," Biophys. J. **99**, 3119–3128 (2010).
53. W. Mohler, A. C. Millard, and P. J. Campagnola, "Second harmonic generation imaging of endogenous structural proteins," Methods **29**, 97–109 (2003).
54. P. J. Campagnola and L. M. Loew, "Second-harmonic imaging microscopy for visualizing biomolecular arrays in cells, tissues and organisms," Nat. Biotechnol. **21**, 1356–1360 (2003).
55. L. T. Cheng, W. Tam, S. R. Marder, A. E. Stiegman, G. Rikken, and C. W. Spangler, "Experimental investigations of organic molecular nonlinear optical polarizabilities. 2. A study of conjugation dependences," J. Phys. Chem. **95**, 10643–10652 (1991).
56. K. Clays and A. Persoons, "Hyper-Rayleigh scattering in solution," Phys. Rev. Lett. **66**, 2980–2983 (1991).
57. M. Szablewski, P. R. Thomas, A. Thornton, D. Bloor, G. H. Cross, J. M. Cole, J. A. K. Howard, M. Malagoli, F. Meyers, J. L. Bredas, W. Wenseleers, and E. Goovaerts, "Highly dipolar, optically nonlinear adducts of tetracyano-p-quinodimethane: synthesis, physical characterization, and theoretical aspects," J. Am. Chem. Soc. **119**, 3144–3154 (1997).
58. T. Verbiest, S. Houbrechts, M. Kauranen, K. Clays, and A. Persoons, "Second-order nonlinear optical materials: recent advances in chromophore design," J. Mater. Chem. **7**, 2175–2189 (1997).
59. N. J. Long, "Organometallic compounds for nonlinear optics—The search for en-light-enment," Angew. Chem.-Int. Edit. **34**, 21–38 (1995).
60. I. R. Whittall, A. M. McDonagh, M. G. Humphrey, and M. Samoc, "Organometallic complexes in nonlinear optics I: second-order nonlinearities," in *Advances in Organometallic Chemistry*, F. G. A. Stone and R. West, eds. (Elsevier, 1998), Vol **42**, pp. 291–362.
61. J. J. Wolff and R. Wortmann, "Organic materials for second-order non-linear optics," Adv. Phys. Org. Chem. **32**, 121–217 (1999).
62. S. Di Bella, "Second-order nonlinear optical properties of transition metal complexes," Chem. Soc. Rev. **30**, 355–366 (2001).
63. B. J. Coe, "Switchable nonlinear optical metallochromophores with pyridinium electron acceptor groups," Accounts Chem. Res. **39**, 383–393 (2006).
64. M. Bates, B. Huang, G. T. Dempsey, and X. W. Zhuang, "Multicolor super-resolution imaging with photo-switchable fluorescent probes," Science **317**, 1749–1753 (2007).
65. M. J. Rust, M. Bates, and X. W. Zhuang, "Sub-diffraction-limit imaging by stochastic optical reconstruction microscopy (STORM)," Nat. Methods **3**, 793–796 (2006).
66. L. Moreaux, O. Sandre, and J. Mertz, "Membrane imaging by second-harmonic generation microscopy," J. Opt. Soc. Am. B **17**, 1685–1694 (2000).
67. P. J. Campagnola, H. A. Clark, W. A. Mohler, A. Lewis, and L. M. Loew, "Second-harmonic imaging microscopy of living cells," J. Biomed. Opt. **6**, 277–286 (2001).
68. M. Nuriya, J. Jiang, B. Nemet, K. B. Eisenthal, and R. Yuste, "Imaging membrane potential in dendritic spines," Proc. Natl. Acad. Sci. USA **103**, 786–790 (2006).
69. D. A. Dombeck, M. Blanchard-Desce, and W. W. Webb, "Optical recording of action potentials with second-harmonic generation microscopy," J. Neurosci. **24**, 999–1003 (2004).
70. Y. R. Shen, "Optical second harmonic generation at interfaces," Annu. Rev. Phys. Chem. **40**, 327–350 (1989).
71. J. I. Dadap, J. Shan, K. B. Eisenthal, and T. F. Heinz, "Second-harmonic Rayleigh scattering from a sphere of centrosymmetric material," Phys. Rev. Lett. **83**, 4045–4048 (1999).
72. J. I. Dadap, J. Shan, and T. F. Heinz, "Theory of optical second-harmonic generation from a sphere of centrosymmetric material: small-particle limit," J. Opt. Soc. Am. B **21**, 1328–1347 (2004).
73. B. Z. Huo, X. H. Wang, S. J. Chang, and M. Zeng, "Second harmonic generation of a single centrosymmetric nanosphere illuminated by tightly focused cylindrical vector beams," J. Opt. Soc. Am. B **29**, 1631–1640 (2012).
74. G. Bachelier, I. Russier-Antoine, E. Benichou, C. Jonin, and P. F. Brevet, "Multipolar second-harmonic generation in noble metal nanoparticles," J. Opt. Soc. Am. B **25**, 955–960 (2008).
75. S. Kujala, B. K. Canfield, M. Kauranen, Y. Svirko, and J. Turunen, "Multipolar analysis of second-harmonic radiation from gold nanoparticles," Opt. Express **16**, 17196–17208 (2008).

76. Y. Zeng, W. Hoyer, J. J. Liu, S. W. Koch, and J. V. Moloney, "Classical theory for second-harmonic generation from metallic nanoparticles," Phys. Rev. B **79**, 235109 (2009).
77. J. Butet, I. Russier-Antoine, C. Jonin, N. Lascoux, E. Benichou, and P. F. Brevet, "Sensing with multipolar second harmonic generation from spherical metallic nanoparticles," Nano Lett. **12**, 1697–1701 (2012).
78. I. Russier-Antoine, E. Benichou, G. Bachelier, C. Jonin, and P. F. Brevet, "Multipolar contributions of the second harmonic generation from silver and gold nanoparticles," J. Phys. Chem. C **111**, 9044–9048 (2007).
79. F. W. Vance, B. I. Lemon, and J. T. Hupp, "Enormous hyper-Rayleigh scattering from nanocrystalline gold particle suspensions," J. Phys. Chem. B **102**, 10091–10093 (1998).
80. M. Chandra and P. K. Das, "Small-particle limit" in the second harmonic generation from noble metal nanoparticles," Chem. Phys. **358**, 203–208 (2009).
81. J. Butet, J. Duboisset, G. Bachelier, I. Russier-Antoine, E. Benichou, C. Jonin, and P. F. Brevet, "Optical second harmonic generation of single metallic nanoparticles embedded in a homogeneous medium," Nano Lett. **10**, 1717–1721 (2010).
82. I. Russier-Antoine, C. Jonin, J. Nappa, E. Benichou, and P. F. Brevet, "Wavelength dependence of the hyper Rayleigh scattering response from gold nanoparticles," J. Chem. Phys. **120**, 10748–10752 (2004).
83. B. K. Canfield, S. Kujala, K. Jefimovs, J. Turunen, and M. Kauranen, "Linear and nonlinear optical responses influenced by broken symmetry in an array of gold nanoparticles," Opt. Express **12**, 5418–5423 (2004).
84. B. K. Canfield, H. Husu, J. Laukkanen, B. F. Bai, M. Kuittinen, J. Turunen, and M. Kauranen, "Local field asymmetry drives second-harmonic generation in noncentrosymmetric nanodimers," Nano Lett. **7**, 1251–1255 (2007).
85. V. K. Valev, N. Smisdom, A. V. Silhanek, B. De Clercq, W. Gillijns, M. Ameloot, V. V. Moshchalkov, and T. Verbiest, "Plasmonic ratchet wheels: switching circular dichroism by arranging chiral nanostructures," Nano Lett. **9**, 3945–3948 (2009).
86. M. J. Huttunen, G. Bautista, M. Decker, S. Linden, M. Wegener, and M. Kauranen, "Nonlinear chiral imaging of subwavelength-sized twisted-cross gold nanodimers (Invited)," Opt. Mater. Express **1**, 46–56 (2011).
87. Y. Zhang, N. K. Grady, C. Ayala-Orozco, and N. J. Halas, "Three-dimensional nanostructures as highly efficient generators of second harmonic light," Nano Lett. **11**, 5519–5523 (2011).
88. S. W. Chan, R. Barille, J. M. Nunzi, K. H. Tam, Y. H. Leung, W. K. Chan, and A. B. Djurisic, "Second harmonic generation in zinc oxide nanorods," Appl. Phys. B **84**, 351–355 (2006).
89. K. Geren, S. W. Liu, H. J. Zhou, Y. Zhang, R. Tian, and M. Xiao, "Second-order susceptibilities of ZnO nanorods from forward second-harmonic scattering," J. Appl. Phys. **105**, 063531 (2009).
90. R. Le Dantec, Y. Mugnier, G. Djanta, L. Bonacina, J. Extermann, L. Badie, C. Joulaud, M. Gerrmann, D. Rytz, J. P. Wolf, and C. Galez, "Ensemble and individual characterization of the nonlinear optical properties of ZnO and $BaTiO_3$ nanocrystals," J. Phys. Chem. C **115**, 15140–15146 (2011).
91. B. E. Urban, J. Lin, O. Kumar, K. Senthilkumar, Y. Fujita, and A. Neogi, "Optimization of nonlinear optical properties of ZnO micro and nanocrystals for biophotonics," Opt. Mater. Express **1**, 658–669 (2011).
92. R. Grange, J. W. Choi, C. L. Hsieh, Y. Pu, A. Magrez, R. Smajda, L. Forro, and D. Psaltis, "Lithium niobate nanowires synthesis, optical properties, and manipulation," Appl. Phys. Lett. **95**, 143105 (2009).
93. F. Dutto, C. Raillon, K. Schenk, and A. Radenovic, "Nonlinear optical response in single alkaline niobate nanowires," Nano Lett. **11**, 2517–2521 (2011).
94. Y. Nakayama, P. J. Pauzauskie, A. Radenovic, R. M. Onorato, R. J. Saykally, J. Liphardt, and P. D. Yang, "Tunable nanowire nonlinear optical probe," Nature **447**, 1098–1101 (2007).
95. Y. Wang, Z. Chen, Z. Z. Ye, and J. Y. Huang, "Synthesis and second harmonic generation response of $KNbO_3$ nanoneedles," J. Cryst. Growth **341**, 42–45 (2012).
96. P. Wnuk, L. Le Xuan, A. Slablab, C. Tard, S. Perruchas, T. Gacoin, J. F. Roch, D. Chauvat, and C. Radzewicz, "Coherent nonlinear emission from a single KTP nanoparticle with broadband femtosecond pulses," Opt. Express **17**, 4652–4658 (2009).
97. E. V. Rodriguez, C. B. de Araujo, A. M. Brito-Silva, V. I. Ivanenko, and A. A. Lipovskii, "Hyper-Rayleigh scattering from $BaTiO_3$ and $PbTiO_3$ nanocrystals," Chem. Phys. Lett. **467**, 335–338 (2009).
98. C. L. Hsieh, R. Grange, Y. Pu, and D. Psaltis, "Three-dimensional harmonic holographic microcopy using nanoparticles as probes for cell imaging," Opt. Express **17**, 2880–2891 (2009).
99. L. Bonacina, Y. Mugnier, F. Courvoisier, R. Le Dantec, J. Extermann, Y. Lambert, V. Boutou, C. Galez, and J. P. Wolf, "Polar $Fe(IO_3)_3$ nanocrystals as local probes for nonlinear microscopy," Appl. Phys. B **87**, 399–403 (2007).
100. J. Extermann, L. Bonacina, E. Cuna, C. Kasparian, Y. Mugnier, T. Feurer, and J. P. Wolf, "Nanodoublers as deep imaging markers for multi-photon microscopy," Opt. Express **17**, 15342–15349 (2009).
101. R. Grange, T. Lanvin, C. L. Hsieh, Y. Pu, and D. Psaltis, "Imaging with second-harmonic radiation probes in living tissue," Biomed. Opt. Express **2**, 2532–2539 (2011).
102. A. V. Kachynski, A. N. Kuzmin, M. Nyk, I. Roy, and P. N. Prasad, "Zinc oxide nanocrystals for nonresonant nonlinear optical microscopy in biology and medicine," J. Phys. Chem. C **112**, 10721–10724 (2008).
103. D. Staedler, T. Magouroux, R. Hadji, C. Joulaud, J. Extermann, S. Schwungi, S. Passemard, C. Kasparian, G. Clarke, M. Gerrmann, R. Le Dantec, Y. Mugnier, D. Rytz, D. Ciepielewski, C. Galez, S. Gerber-Lemaire, L. Juilleratt-Jeanneret, L. Bonacina, and J. P. Wolf, "Harmonic nanocrystals for biolabeling: a survey of optical properties and biocompatibility," ACS Nano **6**, 2542–2549 (2012).
104. C. L. Hsieh, R. Grange, Y. Pu, and D. Psaltis, "Bioconjugation of barium titanate nanocrystals with immunoglobulin G antibody for second harmonic radiation imaging probes," Biomaterials **31**, 2272–2277 (2010).
105. M. Geissbuehler, L. Bonacina, V. Shcheslavskiy, N. L. Bocchio, S. Geissbuehler, M. Leutenegger, I. Marki, J. P. Wolf, and T. Lasser, "Nonlinear correlation spectroscopy (NLCS)," Nano Lett. **12**, 1668–1672 (2012).
106. M. Jacobsohn and U. Banin, "Size dependence of second harmonic generation in CdSe nanocrystal quantum dots," J. Phys. Chem. B **104**, 1–5 (2000).
107. A. V. Baranov, K. Inoue, K. Toba, A. Yamanaka, V. I. Petrov, and A. V. Fedorov, "Resonant hyper-Raman and second-harmonic scattering in a CdS quantum-dot system," Phys. Rev. B **53**, R1721–R1724 (1996).
108. M. Zielinski, D. Oron, D. Chauvat, and J. Zyss, "Second-harmonic generation from a single core/shell quantum dot," Small **5**, 2835–2840 (2009).
109. A. A. Umar, A. H. Reshak, M. Oyama, and K. J. Plucinski, "Fluorescent and nonlinear optical features of CdTe quantum dots," J. Mater. Sci.: Mater. Electron. **23**, 546–550 (2012).
110. R. Chen, S. Crankshaw, T. Tran, L. C. Chuang, M. Moewe, and C. Chang-Hasnain, "Second-harmonic generation from a single wurtzite GaAs nanoneedle," Appl. Phys. Lett. **96**, 051110 (2010).
111. F. Wang, P. J. Reece, S. Paiman, Q. Gao, H. H. Tan, and C. Jagadish, "Nonlinear optical processes in optically trapped InP nanowires," Nano Lett. **11**, 4149–4153 (2011).
112. Y. Pu, R. Grange, C. L. Hsieh, and D. Psaltis, "Nonlinear optical properties of core-shell nanocavities for enhanced second-harmonic generation," Phys. Rev. Lett. **104**, 207402 (2010).
113. Y. Pu, C. L. Hsieh, R. Grange, and D. Psaltis, "Harmonic holography," in *Advances in Imaging and Electron Physics*, P. W. Hawkes, ed. (Elsevier, 2010), Vol **160**, pp. 75–112.
114. O. Masihzadeh, P. Schlup, and R. A. Bartels, "Label-free second harmonic generation holographic microscopy of biological specimens," Opt. Express **18**, 9840–9851 (2010).

115. D. G. Winters, D. R. Smith, P. Schlup, and R. A. Bartels, "Measurement of orientation and susceptibility ratios using a polarization-resolved second-harmonic generation holographic microscope," Biomed. Opt. Express **3**, 2004–2011 (2012).
116. E. Shaffer, P. Marquet, and C. Depeursinge, "Second harmonic phase microscopy of collagen fibers,"Proc. SPIE **7903**, 79030G (2011).
117. K. B. Shi, H. F. Li, Q. Xu, D. Psaltis, and Z. W. Liu, "Coherent anti-Stokes Raman holography for chemically selective single-shot nonscanning 3D imaging," Phys. Rev. Lett. **104**, 093902 (2010).
118. K. B. Shi, P. S. Edwards, J. Hu, Q. Xu, Y. M. Wang, D. Psaltis, and Z. W. Liu, "Holographic coherent anti-Stokes Raman scattering bio-imaging," Biomed. Opt. Express **3**, 1744–1749 (2012).
119. C. L. Hsieh, Y. Pu, R. Grange, G. Laporte, and D. Psaltis, "Imaging through turbid layers by scanning the phase conjugated second harmonic radiation from a nanoparticle," Opt. Express **18**, 20723–20731 (2010).
120. X. Yang, C. L. Hsieh, Y. Pu, and D. Psaltis, "Three-dimensional scanning microscopy through thin turbid media," Opt. Express **20**, 2500–2506 (2012).